LETTER

doi:10.1038/nature23678

Feedback regulation of steady-state epithelial turnover and organ size

Jackson Liang[1], Shruthi Balachandra[1], Sang Ngo[1] & Lucy Erin O'Brien[1]

Epithelial organs undergo steady-state turnover throughout adult life, with old cells being continually replaced by the progeny of stem cell divisions[1]. To avoid hyperplasia or atrophy, organ turnover demands strict equilibration of cell production and loss[2–4]. However, the mechanistic basis of this equilibrium is unknown. Here we show that robustly precise turnover of the adult *Drosophila* intestine[5] arises through a coupling mechanism in which enterocyte apoptosis breaks feedback inhibition of stem cell division. Healthy enterocytes inhibit stem cell division through E-cadherin, which prevents secretion of mitogenic epidermal growth factors (EGFs) by repressing transcription of the EGF maturation factor *rhomboid*. Individual apoptotic enterocytes promote divisions by loss of E-cadherin, which releases cadherin-associated β-catenin (Armadillo in *Drosophila*) and p120-catenin to induce *rhomboid*. Induction of *rhomboid* in the dying enterocyte triggers activation of the EGF receptor (Egfr) in stem cells within a discrete radius. When we blocked apoptosis, E-cadherin-controlled feedback suppressed divisions, and the organ retained the same number of cells. When we disrupted feedback, apoptosis and divisions were uncoupled, and the organ developed either hyperplasia or atrophy. Together, our results show that robust cellular balance hinges on the obligate coupling of divisions to apoptosis, which limits the proliferative potential of a stem cell to the precise time and place at which a replacement cell is needed. In this way, localized cell–cell communication gives rise to tissue-level homeostatic equilibrium and constant organ size.

Throughout an animal's lifetime, mature organs undergo continuous cell turnover yet can maintain the same approximate size. This remarkable ability implies the existence of robust mechanisms to ensure that turnover is zero-sum, with cell production and loss held precisely equal[1,2,4]. In most organs, production of new cells ultimately depends on divisions of resident stem cells. Although much is understood about how excessive or insufficient divisions lead to disease, little is known about how equal rates of division and loss are sustained during the steady-state turnover of healthy tissues.

We investigated the regulation of turnover in the midgut epithelium of adult *Drosophila*[5] (Extended Data Fig. 1a–e). To establish whether production of new cells equals loss of old cells, we measured the kinetics of cell addition and loss in the R4ab region using *escargot>GFP* flp-out labelling (*esg*$^{F/O}$*>GFP*)[6,7] (Fig. 1a–e and Extended Data Fig. 1f, g). Newly added, GFP$^+$ cells increased linearly over time and, after four days, comprised all cells in R4ab. Concomitantly, the total cell number remained near-constant. We conclude that the production of new cells quantitatively equals the loss of old cells.

To investigate the relationship between cell production and loss, we devised a system to manipulate mature enterocytes and simultaneously track divisions of stem cells by combining enterocyte-specific *mexGAL4; GAL80*^{ts} (*mex*^{ts}) with split-*nlsLacZ* clonal labelling[3,8] (Fig. 1f and Extended Data Fig. 2). Using this two-pronged system, we expressed the apoptotic inhibitor *p35* in enterocytes and assessed the impact on stem cell divisions. Blocking enterocyte apoptosis resulted in fewer divisions, as indicated by smaller clones (Fig. 1g–i). Apoptotic inhibition also impeded S phase progression (Fig. 1j), consistent with a previous report[9]. Reduced divisions could be a compensatory means to keep a constant number of total cells. Indeed, the total cell number, as well as physical size and morphology, of apoptosis-inhibited midguts remained

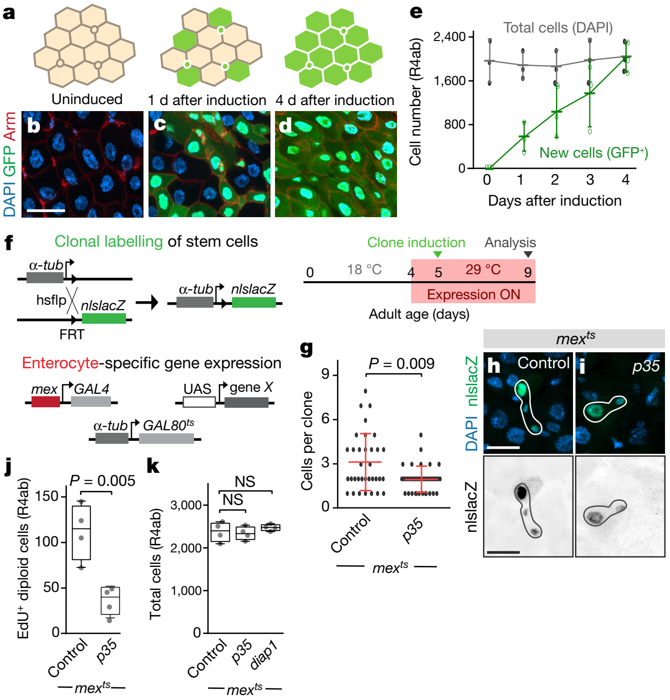

Figure 1 | Enterocyte apoptosis regulates the rate of stem cell division for homeostatic maintenance of total cell number. a–e, Kinetics of midgut epithelial turnover: cartoon (**a**), images (**b**–**d**) and quantification (**e**) of *esg*$^{F/O}$*>GFP* labelling. Progenitors (**a**, small circles) express GFP upon induction; new, but not old, enterocytes (**a**, large hexagons) inherit GFP from progenitors after induction. Quantification of total and GFP$^+$ cells over time shows complete replacement of unlabelled cells by GFP$^+$ cells after four days (**e**). Mean ± s.d.; three midgut R4ab compartments per time point. See Extended Data Fig. 1. **f**, Genetic schema and experimental timeline for tracing stem cell divisions (split-*lacZ* clones) in a background of genetically manipulated enterocytes (*mex*^{ts}). See Extended Data Fig. 2. **g**–**i**, Sizes (**g**) and images (**h**, **i**) of stem cell clones following enterocyte inhibition of apoptosis (*mex*^{ts}*>p35*). Clone sizes are reduced by apoptotic inhibition. Mean ± s.d.; P values by Mann–Whitney U-test; $n = 5$ midguts per genotype. **j**, EdU incorporation in diploid cells is reduced by apoptotic inhibition. **k**, Total cell counts of the R4ab compartment with control or apoptosis-inhibited (*p35* or *diap1*) enterocytes. **j**, **k**, For box-and-whisker plots, the boxes show median, 25th and 75th percentiles, and whiskers are minimum and maximum values; P values by unpaired t-test; NS, not significant; $n = 4$ midguts per genotype. **e**, **g**, **j**, **k**, One of three independent experiments is shown with n numbers as specified for each experiment. Scale bars, 25 μm.

---

[1] Department of Molecular and Cellular Physiology, Stanford University School of Medicine, Stanford, California 94305, USA.

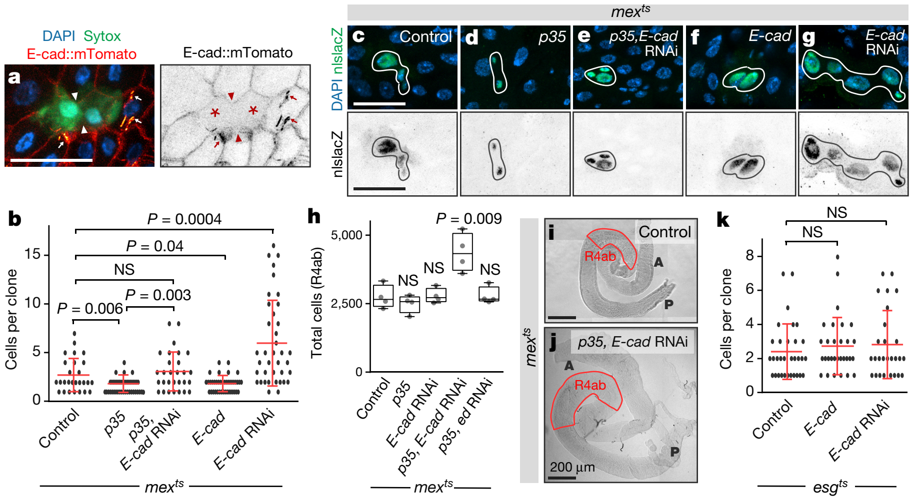

Figure 2 | Homeostatic size control requires *E-cad* on enterocytes, but not on stem cells. a, E-cad::m-Tomato (red-hot LUT) is absent from cell–cell junctions (arrowheads) of dying enterocytes (Sytox^{+}, asterisks). Tracheal autofluorescence appears as bright, red-yellow lines (arrows). **b–g**, Sizes (**b**) and images (**c–g**) of stem cell clones following enterocyte manipulation of *E-cad*, with or without apoptotic inhibition (*p35*; experimental schema in Fig. 1f). Clone sizes are decreased by enterocyte E-cad. **h–j**, Total cell counts (**h**) and whole-organ images (**i**, **j**). Midguts become hyperplastic after enterocyte expression of *p35* combined with RNA interference (RNAi) of *E-cad*, but not after expression of either *p35* or *E-cad* RNAi alone, or co-expression of *p35* and *ed* RNAi. A, anterior; P, posterior. Box-and-whisker plots as in Fig. 1j, k; *P* values by unpaired *t*-test; $n = 4$ midguts per genotype. See Extended Data Figs 3a, 5. **k**, Sizes of stem cell clones are unchanged by manipulation of *E-cad* in stem and enteroblast cells. Experimental schema similar to Fig. 1f, but using stem cell and/or enteroblast *esg*^{ts}*GAL4*. **b**, **k**, Mean ± s.d.; *P* values by Mann–Whitney *U*-test; $n = 4, 5, 4, 5$ and 4 midguts from left to right (**b**) and $n = 5, 3$ and 5 midguts from left to right (**k**). **b**, **h**, **k**, One of three independent experiments is shown with *n* numbers as specified for each experiment. Scale bars, 25 μm or as indicated.

normal (Fig. 1k and Extended Data Figs 3a, 4a, b, d, e). These findings imply that enterocyte apoptosis and stem cell division are homeostatically coupled to maintain a constant cell number and organ size.

We sought to determine this coupling mechanism. The cell–cell adhesion protein E-cadherin (E-cad) drew our attention because in the mouse intestine, enterocyte E-cad represses stem cell divisions[10], and in other epithelia, E-cad is degraded by caspases during apoptosis[11]. In the *Drosophila* midgut, we found that E-cad::mTomato was largely eliminated from the interfaces of dying, Sytox^{+} enterocytes (Fig. 2a), indicating that apoptotic enterocytes lose junctional E-cad.

To investigate whether E-cad couples divisions to apoptosis, we depleted *E-cad* (also known as *shg*) in apoptosis-inhibited enterocytes and assessed stem cell divisions by measuring clones. Depletion of enterocyte *E-cad* did not disrupt epithelial architecture or integrity (Extended Data Fig. 4a, c, d, f–j). It did, however, prevent the reduction in stem cell divisions that would otherwise have occurred following apoptotic inhibition (Fig. 2b–e). Consequently, the total cell number increased by 70%, and organs became markedly hyperplastic (Fig. 2h–j and Extended Data Fig. 3a). These effects were specific to E-cad, because the depletion of another cell–cell adhesion protein, *echinoid*, did not affect cell number (Fig. 2h). Without apoptotic inhibition, *E-cad* depletion caused excess divisions, but not hyperplasia (Fig. 2b), which was probably related to other, tissue-level effects (Extended Data Fig. 5). Conversely, *E-cad* overexpression suppressed divisions (Fig. 2f). These findings show that in apoptosis-inhibited midguts, homeostatic suppression of stem cell divisions requires enterocyte E-cad.

Because E-cad functions as an intercellular homodimer, we considered whether enterocyte E-cad acts by dimerizing with stem cell E-cad[12,13]. Notably, we found that manipulation of *E-cad* in stem and enteroblast cells did not alter the rate of stem cell divisions, at least as measured by four-day clones (Fig. 2k). Therefore, enterocyte E-cad does not act through stem cell E-cad, but through a distinct intermediary.

We sought to identify this intermediary. Notable candidates included four E-cad-associated pathways: Wingless/Wnt, Hippo, Jak–Stat and Egfr. To assess whether these pathways act downstream of enterocyte E-cad, we investigated whether *E-cad* knockdown induced pathway-specific target genes and reporters (Extended Data Fig. 6a–j). *E-cad* knockdown did not induce Wingless or Hippo targets, Jak–Stat pathway components or Stat signalling in stem cells, although Stat activity in enterocytes was mildly increased. By contrast, *E-cad* knockdown induced activation of Egfr targets in diploid cells, which probably included presumptive stem cells.

We therefore analysed the functional relationship between enterocyte E-cad, stem cell Egfr and organ size control. In the *Drosophila* midgut, a specific readout of Egfr activation is diphosphorylation of the effector kinase Erk (dpErk); endogenous diphosphorylation of Erk requires Egfr and occurs primarily in stem cells[14–17] (Fig. 3d, e and Extended Data Figs 3b, 6k). We found that enterocyte *E-cad* knockdown caused the number of dpErk^{+} stem cells to increase, whereas overexpression caused dpErk^{+} stem cells to decrease (Fig. 3a–c and Extended Data Fig. 3b). Furthermore, Egfr was necessary for the excess divisions and organ hyperplasia that were induced by knockdown of *E-cad* in apoptosis-inhibited enterocytes (Fig. 3f–g and Extended Data Fig. 3a). Therefore, enterocyte E-cad inhibits stem cell Egfr to mediate homeostatic control of cell number and organ size.

We next investigated how enterocyte E-cad controls Egfr on stem cells. One possible mechanism involves a direct, E-cad–Egfr interaction[18]; another involves a dispersed signal. To examine these possibilities, we generated isolated, GFP-marked enterocytes that were depleted of *E-cad*. Measuring the spatial distribution of dpErk^{+} stem cells surrounding each mutant enterocyte (Fig. 3h–j), we found a zone of strong Egfr activation within 25 μm and a second zone of weak activation from 25–50 μm (Fig. 3k). The spatial extent of these zones suggests the involvement of a dispersed signal.

Consistent with a dispersed signal, two enterocyte-derived Egfs, *spitz* (*spi*) and *keren* (*krn*), were necessary for organ hyperplasia caused by the loss of *E-cad* in apoptosis-inhibited enterocytes (Fig. 3g and Extended Data Fig. 3a). However, *spi* and *krn* were not induced by *E-cad* knockdown (Fig. 4a). The visceral muscle Egf *vein*, the modulators of Egf *Star* and *argos*, and *egfr* itself were also unaffected. By contrast, the obligate Egf protease *rhomboid* (*rho*) was markedly induced by *E-cad* knockdown and repressed by *E-cad* overexpression.

Rho operates within Egf-producing cells, where it cleaves Egf precursors for secretion[19]. We found that E-cad repressed the transcriptional

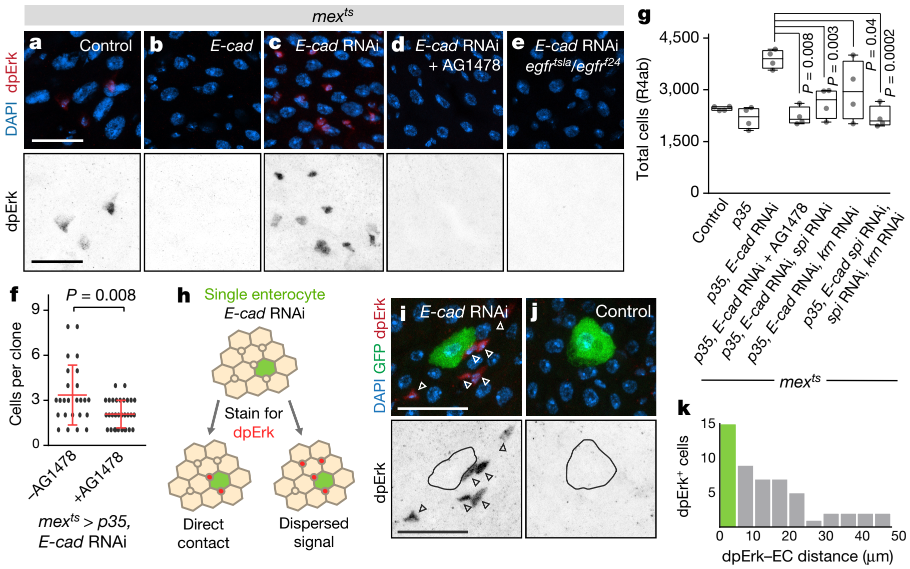

Figure 3 | Enterocyte E-cad inhibits stem cell Egfr through a dispersed signal for homeostatic size control. a–**e**, Immunostaining of activated, diphosphorylated Erk (dpErk) following enterocyte manipulation of *E-cad*, without or with Egfr inhibition (AG1478, *egfr^{tlsa}*). Erk activation in stem cells (Extended Data Fig. 6k) is repressed by *E-cad* and requires Egfr. See Extended Data Fig. 3b. **f**, Sizes of stem cell clones after induction of enterocyte *p35* and *E-cad* RNAi, without or with AG1478. Egfr inhibition suppresses stem cell divisions. Mean ± s.d.; *P* values by Mann–Whitney *U*-test; $n = 4$ midguts per condition. **g**, Total cell counts. Midgut hyperplasia (*mex^{ts}>p35*, *E-cad* RNAi) requires Egfr and enterocyte *spi* and *krn*. Box-and-whisker plots as in Fig. 1j, k; *P* values by unpaired *t*-test compared to control; $n = 4$ midguts per condition. See Extended Data Fig. 3a. **h**, The spatial distribution of dpErk cells around a single, *E-cad*-RNAi-expressing enterocyte distinguishes direct and dispersed activation mechanisms. **i**, dpErk^{+} cells are both directly adjacent to and dispersed from GFP-marked, *E-cad*-RNAi-expressing enterocytes, consistent with a dispersed mechanism. **j**, dpErk^{+} cells are infrequent near marked control enterocytes. **k**, Distances between dpErk^{+} cells and *E-cad*-RNAi-expressing enterocytes (EC). $n = 4$ midguts (53 dpErk^{+} cells total), five day induction. Green bar (**k**) represents dpErk^{+} cells directly adjacent to enterocytes (0 μm). **f**, **g**, **k**, One of three independent experiments is shown with *n* numbers as specified for each experiment. Scale bars, 25 μm.

reporter *rho-lacZ* specifically in enterocytes (Extended Data Fig. 7c, d, f). Overexpression of *rho* in enterocytes caused dpErk^{+} cells and phospho-histone H3^{+} cells to increase; conversely, *rho* depletion caused dpErk^{+} cells to virtually disappear (Extended Data Figs 3b, 7m–o, s). Furthermore, combined depletion of *rho* and *E-cad* precluded the hyperactivation of Erk caused by depletion of *E-cad* alone (Fig. 4b, c). Together, these results imply that enterocyte E-cad inhibits stem cell Egfr by preventing Egf secretion through the repression of *rho*.

We then investigated whether the E-cad–Rho–Egfr pathway couples stem cell divisions to enterocyte apoptosis. If this is the case, then: (1) apoptotic enterocytes, which lose E-cad, should upregulate *rho*; (2) loss of E-cad in apoptotic enterocytes should underlie stem cell Egfr activation; and (3) exogenous manipulation of *rho* should alter organ

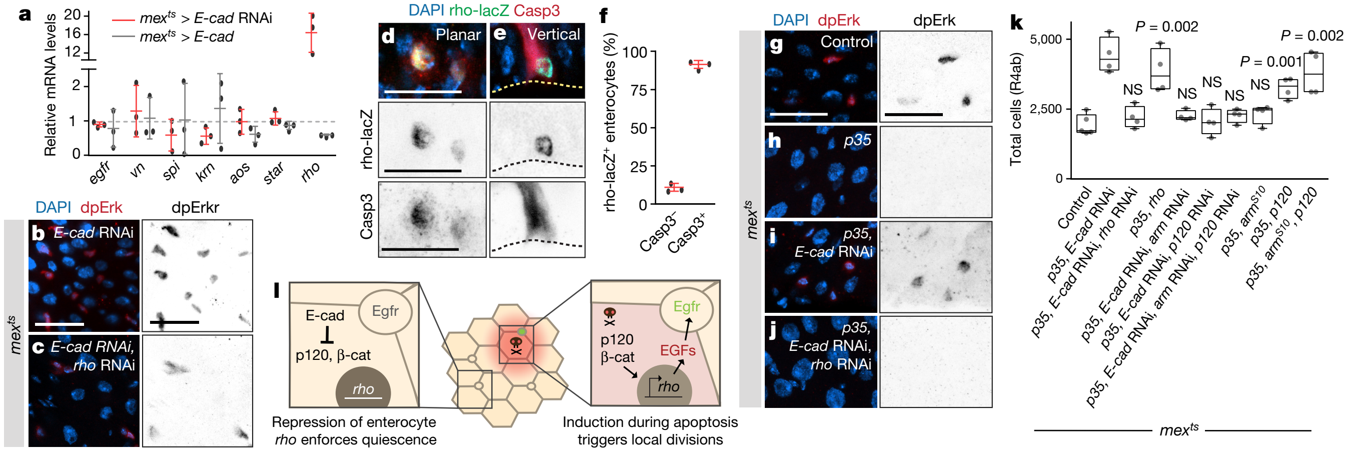

Figure 4 | Enterocyte apoptosis activates stem cell division by disrupting E-cad-controlled inhibition of *rhomboid*. a, qPCR of whole midgut mRNA following enterocyte-specific *E-cad* manipulation. *E-cad* represses *rho* but not Egfs (*vn*, *spi*, *krn*) or other Egf-related factors (*egfr*, *aos*, *star*). Control: dotted line. Mean ± s.d.; three biological replicates per condition. **b**, **c**, Enterocyte *rho* is required for Erk hyperactivation following depletion of enterocyte *E-cad*. See Extended Data Fig. 3b. **d**–**f**, *rho-lacZ* induction during physiological apoptosis. Immunostaining of β-gal and activated caspase-3 (Casp3) mark the same enterocytes. Images show different fields in planar (**d**) and vertical (**e**) sections; dotted line in **e** indicates basal. **f**, Percentage of Casp3^{+}, *rho-lacZ*$^{+}$ enterocytes six days after eclosion. Mean ± s.d. of three independent experiments with $n = 3$ midguts per experiment; $n = 188$ enterocytes total. **g**–**j**, Erk activation is suppressed by apoptotic inhibition and depends on *E-cad* and *rho*. See Extended Data Fig. 3b. **k**, Total cell counts. Hyperplasia of *mex^{ts}>p35*, *E-cad* RNAi midguts requires *rho*, *arm* and *p120*. Hyperplasia is induced by either *rho* or *p120* alone. Box-and-whisker plots as in Fig. 1j, k; *P* values by unpaired *t*-test compared to control; $n = 5$ midguts (control) and 4 midguts (all other genotypes); one of three independent experiments is shown. See Extended Data Fig. 3a. **l**, Model for steady-state equilibrium. Scale bars, 25 μm.

size. We investigated each prediction. First, *rho-lacZ* predominantly marked apoptotic enterocytes during normal turnover (Fig. 4d–f). By comparison, the cardinal injury signal *upd3* (refs 20, 21) rarely marked apoptotic enterocytes; *upd3* was also dispensable for Egfr activation (Extended Data Figs 6l, 7i and Supplementary Discussion). Therefore, *rho* is silenced in healthy enterocytes but upregulated in enterocytes undergoing physiological apoptosis.

Second, we blocked enterocyte apoptosis and examined stem cell Egfr activation. Erk-activated stem cells were almost completely absent following apoptotic inhibition but were restored, in a *rho*-dependent manner, by additional depletion of enterocyte *E-cad* (Fig. 4g–j and Extended Data Fig. 3b). These results demonstrate that the loss of E-cad in apoptotic enterocytes underlies Egfr activation in stem cells.

Third, we manipulated enterocyte *rho* and measured cell number and organ size. Overexpression of *rho* in apoptosis-inhibited enterocytes led to organ hyperplasia (Fig. 4k and Extended Data Fig. 3a). Conversely, loss of *rho* in apoptosis-competent enterocytes resulted in organ atrophy (Extended Data Fig. 8). Moreover, combined loss of both *rho* and *E-cad* in apoptosis-inhibited enterocytes prevented the hyperplasia that would have resulted from the loss of *E-cad* alone (Fig. 4k and Extended Data Fig. 3a). These results show that downstream of E-cad, *rho* is the pivot point that balances division and apoptosis to sustain cellular equilibrium.

Finally, we investigated how E-cad controls *rho* expression by examining three transcription factors whose nuclear localization is precluded by binding to junctional E-cad: β-catenin (Armadillo (Arm) in *Drosophila*), p120-catenin (p120) and Yap (Yorkie (Yki) in *Drosophila*)[22]. *arm* and *p120*, but not *yki*, were required in *E-cad* knockdown enterocytes for induction of *rho* and hyperactivation of stem cell Egfr (Extended Data Figs 3b, 7a, g–l). In addition, *arm* and *p120* were required for organ hyperplasia following combined *E-cad* knockdown and apoptotic inhibition (Fig. 4k and Extended Data Fig. 3a). Conversely, overexpression of *p120*, but not activated arm^{S10}, was sufficient for *rho* induction, Egfr hyperactivation and organ hyperplasia (Extended Data Figs 3b, 7b–f, p–r). Therefore, E-cad controls *rho* by inhibiting p120 and Arm, probably through physical sequestration at cell junctions.

Our results demonstrate that steady-state turnover is not driven by constitutive cycling of stem cells. Rather, healthy enterocytes enforce a default state of stem cell quiescence, while sporadic, apoptotic enterocytes trigger replacement divisions (Fig. 4l). Because divisions are coupled to apoptosis, turnover remains zero-sum over time.

The molecular mechanism of coupling suggests a simple model for how, during continuous turnover, total cell number is held constant with such robust precision. Apoptotic enterocytes trigger stem cell divisions through loss of E-cad, which induces *rho* to permit secretion of mitogenic Egfs. Crucially, a single enterocyte can efficiently activate Egfr on stem cells within an around 25-μm radius (Fig. 3k). We propose that this local zone of activation enables organ size homeostasis. If, by chance, stem cells produce excess enterocytes, the physical spacing of the stem cells would increase; consequently, fewer stem cells would reside in the activation zone of the next dying enterocyte, which would lead to fewer divisions. Similarly, insufficient production of enterocytes would place more stem cells in the activation zone, which would lead to more divisions. We propose that the radii of individual activation zones, when integrated over the entire epithelium, sets total cell number and organ size. In this way, localized cell–cell communication can give rise to tissue-level homeostatic equilibrium.

Online Content Methods, along with any additional Extended Data display items and Source Data, are available in the online version of the paper; references unique to these sections appear only in the online paper.

Received 12 September 2016; accepted 25 July 2017.

1. Leblond, C. P. & Stevens, C. E. The constant renewal of the intestinal epithelium in the albino rat. *Anat. Rec.* **100,** 357–377 (1948).
2. Pellettieri, J. & Sánchez Alvarado, A. Cell turnover and adult tissue homeostasis: from humans to planarians. *Annu. Rev. Genet.* **41,** 83–105 (2007).
3. O'Brien, L. E., Soliman, S. S., Li, X. & Bilder, D. Altered modes of stem cell division drive adaptive intestinal growth. *Cell* **147,** 603–614 (2011).
4. O'Brien, L. E. & Bilder, D. Beyond the niche: tissue-level coordination of stem cell dynamics. *Annu. Rev. Cell Dev. Biol.* **29,** 107–136 (2013).
5. Apidianakis, Y., Tamamouna, V., Teloni, S. & Pitsouli, C. in *Advances in Insect Physiology* Vol. 52 (ed. Ligoxygakis, P.) 139–178 (Academic, 2017).
6. Jiang, H. *et al.* Cytokine/Jak/Stat signaling mediates regeneration and homeostasis in the *Drosophila* midgut. *Cell* **137,** 1343–1355 (2009).
7. Buchon, N. *et al.* Morphological and molecular characterization of adult midgut compartmentalization in *Drosophila*. *Cell Rep.* **3,** 1725–1738 (2013).
8. Harrison, D. A. & Perrimon, N. Simple and efficient generation of marked clones in *Drosophila*. *Curr. Biol.* **3,** 424–433 (1993).
9. Takeishi, A. *et al.* Homeostatic epithelial renewal in the gut is required for dampening a fatal systemic wound response in *Drosophila*. *Cell Rep.* **3,** 919–930 (2013).
10. Hermiston, M. L. & Gordon, J. I. *In vivo* analysis of cadherin function in the mouse intestinal epithelium: essential roles in adhesion, maintenance of differentiation, and regulation of programmed cell death. *J. Cell Biol.* **129,** 489–506 (1995).
11. Steinhusen, U. *et al.* Cleavage and shedding of E-cadherin after induction of apoptosis. *J. Biol. Chem.* **276,** 4972–4980 (2001).
12. Maeda, K., Takemura, M., Umemori, M. & Adachi-Yamada, T. E-cadherin prolongs the moment for interaction between intestinal stem cell and its progenitor cell to ensure Notch signaling in adult *Drosophila* midgut. *Genes Cells* **13,** 1219–1227 (2008).
13. Choi, N. H., Lucchetta, E. & Ohlstein, B. Nonautonomous regulation of *Drosophila* midgut stem cell proliferation by the insulin-signaling pathway. *Proc. Natl Acad. Sci. USA* **108,** 18702–18707 (2011).
14. Biteau, B. & Jasper, H. EGF signaling regulates the proliferation of intestinal stem cells in *Drosophila*. *Development* **138,** 1045–1055 (2011).
15. Buchon, N., Broderick, N. A., Kuraishi, T. & Lemaitre, B. *Drosophila* EGFR pathway coordinates stem cell proliferation and gut remodeling following infection. *BMC Biol.* **8,** 152 (2010).
16. Jiang, H., Grenley, M. O., Bravo, M. J., Blumhagen, R. Z. & Edgar, B. A. EGFR/Ras/MAPK signaling mediates adult midgut epithelial homeostasis and regeneration in *Drosophila*. *Cell Stem Cell* **8,** 84–95 (2011)
17. Strand, M. & Micchelli, C. A. Regional control of *Drosophila* gut stem cell proliferation: EGF establishes GSSC proliferative set point & controls emergence from quiescence. *PLoS ONE* **8,** e80608 (2013).
18. Qian, X., Karpova, T., Sheppard, A. M., McNally, J. & Lowy, D. R. E-cadherin-mediated adhesion inhibits ligand-dependent activation of diverse receptor tyrosine kinases. *EMBO J.* **23,** 1739–1748 (2004).
19. Shilo, B. Z. Developmental roles of Rhomboid proteases. *Semin. Cell Dev. Biol.* **60,** 5–9 (2016).
20. Zhou, F., Rasmussen, A., Lee, S. & Agaisse, H. The UPD3 cytokine couples environmental challenge and intestinal stem cell division through modulation of JAK/STAT signaling in the stem cell microenvironment. *Dev. Biol.* **373,** 383–393 (2013).
21. Osman, D. *et al.* Autocrine and paracrine unpaired signaling regulate intestinal stem cell maintenance and division. *J. Cell Sci.* **125,** 5944–5949 (2012).
22. McCrea, P. D. & Gottardi, C. J. Beyond β-catenin: prospects for a larger catenin network in the nucleus. *Nat. Rev. Mol. Cell Biol.* **17,** 55–64 (2016).

Supplementary Information is available in the online version of the paper.

Acknowledgements J.L. was supported by NSF GRFP DGE-114747 and NIH T32GM007276. This work was supported by NIH R03DK104027 and R01GM116000-01A1 to L.E.O. Confocal microscopy was performed at the Stanford Beckman Cell Sciences Imaging Facility (NIH 1S10OD01058001A1). We thank D. Bilder for the Caspase-3 antibody; the Developmental Studies Hybridoma Bank for other antibodies; D. Bilder, B. Edgar, M. Fuller, H. Jiang, B. Ohlstein, C. Thummel, A. Orian, the Bloomington *Drosophila* Stock Center (NIH P40OD018537), the TRiP at Harvard Medical School (NIH/NIGMS R01-GM084947) and the Vienna *Drosophila* Resource Center (http://stockcenter.vdrc.at/control/main) for fly stocks; J. Axelrod, M. Goodman, M. Fuller, W. J. Nelson, R. Nusse, M. Krasnow, T. Nystul and D. Fox for comments on the manuscript; and M. Mirvis, B. Benham-Pyle, N. Pierce and D. Gordon for helpful discussions.

Author Contributions J.L. and L.E.O. designed all experiments and wrote the manuscript. J.L. and S.N. dissected and immunostained tissue samples. J.L., S.B. and S.N. performed confocal microscopy on tissue samples. J.L. performed qPCR assays, feeding assays and genetic crosses. J.L. also performed all quantitative analysis of microscopy data (for example, cell numbers, clone sizes, cell distances) and all statistical analysis.

Author Information Reprints and permissions information is available at www.nature.com/reprints. The authors declare no competing financial interests. Readers are welcome to comment on the online version of the paper. Publisher's note: Springer Nature remains neutral with regard to jurisdictional claims in published maps and institutional affiliations. Correspondence and requests for materials should be addressed to L.E.O. (lucye@stanford.edu).

Reviewer Information *Nature* thanks B. Edgar, R. Xi and Y. Yamashita for their contribution to the peer review of this work.

METHODS

***Drosophila* husbandry.** Crosses using the GAL4/$GAL80^{ts}$ system were performed at 18 °C. Upon eclosion, adult flies were kept at 18 °C for four days, unless indicated otherwise. On adult day 4, flies were temperature shifted to 29 °C to inactivate $GAL80^{ts}$ and induce GAL4-mediated expression. Midguts were collected for immunostaining four days after induction, unless specified otherwise in the figure caption. All other crosses were performed at 25 °C; refer to figure legends for individual time point information. Adult female flies were used in all experiments. See Supplementary Table 1 for experimental genotypes in all figures.

Fly stocks. The following stocks were obtained from the Bloomington Stock Center: $y,w;shg^{mTomato}$ (ref. 23), UAS-*shotgun* RNAi (TRiP.HMS00693, TRiP.JF02769 and TRiP.GL00646), UAS-*echinoid* RNAi (TRiP.GL00648), UAS-*rhomboid* RNAi (TRiP.JF03106), UAS-*spitz* RNAi (TRiP.HMS01120), UAS-*armadillo* RNAi (TRiP.JF01251), UAS-*p120ctn* RNAi (TRiP.HMC03276), UAS-*yorkie* RNAi (TRiP.JF03119), UAS-*unpaired3* RNAi (TRiP.HM05061), UAS-*hisH2A:RFP*, UAS-*p35*, UAS-*diap1*, UAS-*rhomboid*, UAS-$armadillo^{S10}$, UAS-*p120ctn*, $Egfr^{f24}/T(2;3)TSTL$, $Egfr^{tsla}/T(2;3)TSTL$, *cycE-lacZ* and *10×Stat-GFP.* UAS-*keren* RNAi (KK104299) and UAS-*armadillo* RNAi (KK107344) were obtained from the Vienna *Drosophila* Resource Center. The following stocks were gifts: *esg* flp-out line[6] (from B. Edgar), $mexGAL4$[24] (from C. Thummel), UAS-$E\text{-}cadherin^{DEFL}$ (from M. Fuller), rho^{X81} (*rho-lacZ*) and *Upd3.1-lacZ* (from H. Jiang), UAS-*groucho* (from A. Orian). Other stocks used: *esgGAL4, y w hsflp; X-15-29 w*$^{+}$ ('split-*lacZ*')[8], *y w; y*$^{+}$ *X-15-33* ('split-*lacZ*')[8], *w UAS-CD8:GFP hsflp; tubGAL4; FRT82 tubGAL80, w; FRT82* (used in our previous study[3]). Detailed information on *Drosophila* genes and stocks is available from FlyBase (http://flybase.org/).

Immunohistochemistry and microscopy. Samples were fixed, immunostained and mounted as previously described[3]. Primary antibodies: mouse anti-β-galactosidase (1:400, Promega Z3781), mouse anti-Armadillo (1:100, DSHB N27A1), rabbit anti-cleaved caspase-3 (1:200, Cell Signaling, gift from D. Bilder[3]), rabbit anti-dpErk (1:400, Cell Signaling 4370P), goat anti-HRP-Cy3 (1:100, Cappel), which stains stem cells and enteroblasts[3], mouse anti-Coracle (1:50, DSHB C615.16), mouse anti-Discs large C615.16 (1:50, DSHB 4F3) and rabbit anti-phospho-histone H3, Ser10 (1:1,000, EMD Millipore). Secondary antibodies: Alexa Fluor 488-, 555- or 647-conjugated donkey anti-rabbit or anti-mouse IgGs (1:800, LifeTechnologies A31570, A11001 and A21244). Nuclei were stained with DAPI (LifeTechnologies, 1:1,000). Actin was stained with SiR-Actin (1:500, Spirochrome) or Alexa 647-conjugated phalloidin (1:100, LifeTechnologies). Samples were mounted in ProLong (LifeTechnologies). Imaging of samples was performed on a Leica SP8 confocal microscope, with serial optical sections taken at 3.5-μm intervals through the entirety of whole-mounted, immunostained midguts. Representative images are shown in all panels.

Regionalization of the adult midgut; cell counts and size measurements of the R4ab (P1–2) compartment. The *Drosophila* midgut is compartmentalized along its proximal–distal axis. Each compartment exhibits a characteristic digestive physiology, gene expression pattern and stem cell division rate[7,25]. In general, stem cell clones do not cross compartment boundaries[25]. Our study focused specifically on two adjacent compartments, known alternatively as R4ab or P1–2, which comprise the major region of nutrient absorption. We observed that R4ab consistently exhibited complete cellular turnover between adult days 4 and 8, as indicated by $esg^{F/O}$ labelling (Fig. 1a–e and Extended Data Fig. 1f, g). Other midgut compartments exhibited variable, incomplete turnover during the same time period, consistent with previous reports, and these other compartments were not analysed in this study.

To perform total cell counts of R4ab, this region was first identified in confocal image stacks using morphological landmarks[7] (Extended Data Fig. 1b–e, g) and digitally isolated in Fiji. Bitplane Imaris software algorithms were applied to generate three-dimensional organ reconstructions and comprehensively count individual cell nuclei by mapping DAPI signals to Imaris surface objects. For analysis of $esg^{F/O}$ midguts, GFP^{+} cells were additionally counted by mapping DAPI/GFP colocalization signals to Imaris surface objects. R4ab lengths were measured by a spline through the centre of individual midguts in Fiji.

split-*lacZ* clone induction and analysis. Flies were raised at 18 °C and shifted to 29 °C four days after eclosion. split-*lacZ* clone induction[8] was performed by subjecting flies to two 30-min, 38.5 °C heat shocks separated by a 5-min chill on ice. Four days after clone induction, midguts were immunostained and clones in the R4ab region were identified and analysed by visual examination of serial confocal sections. Clones in regions outside R4ab were excluded from analysis. Clone size was measured as the number of contiguous cells in one discrete clone, as previously described[3]. No labelled cells were observed in the absence of the 38.5 °C heat shock.

To ensure that clone counts exclusively comprised stem cell clones and excluded any non-stem cell (transient) clones that were directly labelled by the heat shock, our split-*lacZ* clonal analyses incorporated two, redundant safeguards. First, a four-day chase period was included between heat-shock induction and subsequent clonal analysis. Enteroblasts/enterocytes that were directly labelled by the heat shock would have been lost during the subsequent chase period. Confirming that transient clones were nearly absent, only 1–3 single-labelled enterocytes were observed per midgut R4ab region after the four-day chase. As a second safeguard, all single-labelled enterocytes were excluded from our clone counts. This induction protocol resulted in an average of 6–8 clones per midgut R4ab gut region, depending on experimental genotype.

EdU labelling. Flies were fed yeast paste prepared with 1 mg ml^{-1} EdU (5-ethynyl-2′-deoxyuridine, Invitrogen) dissolved in water. After two days, tissues were fixed as described above and stained for EdU using the Click-iT EdU kit (Invitrogen) based on the manufacturer's protocol.

Sytox staining. Sytox Green (ThermoFisher, 5 mM in DMSO) or Sytox Orange (ThermoFisher, 5 mM in DMSO) was diluted 1:5,000 in 5% sucrose. Sytox solution was fed to flies in an empty vial for 5–6 h (ref. 26), after which midguts were dissected and mounted in ProLong (LifeTechnologies). Because Sytox is incompatible with fixation, live organs were imaged immediately after mounting.

MARCM clone induction. MARCM clone inductions[27] were performed by subjecting flies to two 30-min, 38.5 °C heat shocks separated by a 5-min chill on ice. For single-enterocyte MARCM clones, flies were dissected five days after induction and terminal clones consisting of one GFP^{+} enterocyte (identified by its polyploid nucleus) were selected for analysis. GFP^{+} enterocytes were excluded from analysis if another GFP^{+} clone was present within an 80-μm radius. Fiji was used to measure the distance between the plasma membrane of the nearest GFP^{+} enterocyte and the centre of dpErk^{+} stem cells within a 60-μm radius. For mosaic analyses of multi-cell MARCM clones, flies were fed Sytox three days after induction and dissected. The proportion of labelled clone cells (GFP^{+}) that were also Sytox^{+} was quantified.

AG1478 drug treatment. Stocks of AG1478 (Sigma-Aldrich) were dissolved in EtOH and subsequently diluted in dH_2O to reach a working concentration of 100 μM AG1478 (in 0.02% EtOH). This 100 μM stock solution was used to prepare yeast paste, which was fed to flies as a supplement to their standard cornmeal–molasses diet for the duration of induced gene expression.

Smurf assay. Smurf assays were conducted by feeding adult flies yeast paste containing 2.5% Brilliant Blue FCF (Sigma) and scoring flies for leakage of dye into the abdomen. Flies were scored as 'non-Smurf' if the blue dye was confined to the gastrointestinal tract and 'Smurf' if the blue dye leaked outside the gastrointestinal tract. As a positive control, flies were fed dye in conjunction with 1% SDS.

qRT–PCR. mRNA was extracted from midguts (five midguts per biological replicate) followed by cDNA synthesis with Invitrogen SuperStrand III First Script Super Mix (Invitrogen). Real-time PCR was performed using the relative standard curve method with SYBR GreenER Supermix (Invitrogen) on a StepOnePlus ABI machine. Each biological replicate was assessed in three technical replicate experiments. Expression levels were normalized to $mexGAL4^{ts}$>*CD4-GFP* midguts; *mef2* transcripts were used as a reference[3]. Primer sequences (Supplementary Table 2) were from refs 16 and 28 and from FlyPrimerBank (http://www.flyrnai.org/). See Supplementary Table 2 for the full primer list.

Statistical analysis. All statistical analyses were performed using Graphpad Prism 6. For comparisons of clone size distributions, unpaired two-tailed Mann–Whitney *U*-tests were used to assess statistical significance. (Clone size distributions are non-normal, independent and derived from a simple random sample.) For comparisons of cell numbers and gut length, unpaired two-tailed *t*-tests were used to assess statistical significance. (Organ cell number and size distributions are normal, independent and derived from a simple random sample.) For comparisons of *rho* gene expression, unpaired two-tailed *t*-tests were used to assess statistical significance. For all box-and-whisker plots: boxes are 25th percentile, median and 75th percentile. Whiskers are maximum and minimum values.

Study design. Sample sizes were chosen based on our previous study[3], which also characterized changes in organ cell number and clone sizes. In split-*lacZ* experiments, single enterocyte clones were excluded from analysis. No other exclusion criteria were applied. No sample randomization or blinding was performed, although automated, Imaris-based computer algorithms were used to analyse and quantify most of the data in this study.

Data availability. The authors declare that all quantitative data supporting the findings of this study are available as Source Data. Source Data for all graphs in Figs 1–4 and Extended Data Figs 3, 5–8 are provided.

23. Huang, J., Zhou, W., Dong, W., Watson, A. M. & Hong, Y. From the cover: directed, efficient, and versatile modifications of the *Drosophila* genome by genomic engineering. *Proc. Natl Acad. Sci. USA* **106,** 8284–8289 (2009).
24. Chen, H., Zheng, X. & Zheng, Y. Age-associated loss of lamin-B leads to systemic inflammation and gut hyperplasia. *Cell* **159,** 829–843 (2014).

25. Marianes, A. & Spradling, A. C. Physiological and stem cell compartmentalization within the *Drosophila* midgut. *eLife* **2,** e00886 (2013).
26. Kolahgar, G. *et al.* Cell competition modifies adult stem cell and tissue population dynamics in a JAK–STAT-dependent manner. *Dev. Cell* **34,** 297–309 (2015).
27. Lee, T. & Luo, L. Mosaic analysis with a repressible cell marker for studies of gene function in neuronal morphogenesis. *Neuron* **22,** 451–461 (1999).
28. Shaw, R. L. *et al.* The Hippo pathway regulates intestinal stem cell proliferation during *Drosophila* adult midgut regeneration. *Development* **137,** 4147–4158 (2010).
29. Micchelli, C. A. & Perrimon, N. Evidence that stem cells reside in the adult *Drosophila* midgut epithelium. *Nature* **439,** 475–479 (2006).
30. Ohlstein, B. & Spradling, A. The adult *Drosophila* posterior midgut is maintained by pluripotent stem cells. *Nature* **439,** 470–474 (2006).
31. O'Brien, L. E. Regional specificity in the *Drosophila* midgut: setting boundaries with stem cells. *Cell Stem Cell* **13,** 375–376 (2013).
32. Rera, M. *et al.* Modulation of longevity and tissue homeostasis by the *Drosophila* PGC-1 homolog. *Cell Metab.* **14,** 623–634 (2011).
33. Daniels, D. L. & Weis, W. I. β-catenin directly displaces Groucho/TLE repressors from Tcf/Lef in Wnt-mediated transcription activation. *Nat. Struct. Mol. Biol.* **12,** 364–371 (2005).
34. Zhang, T. & Du, W. Groucho restricts rhomboid expression and couples EGFR activation with R8 selection during *Drosophila* photoreceptor differentiation. *Dev. Biol.* **407,** 246–255 (2015).

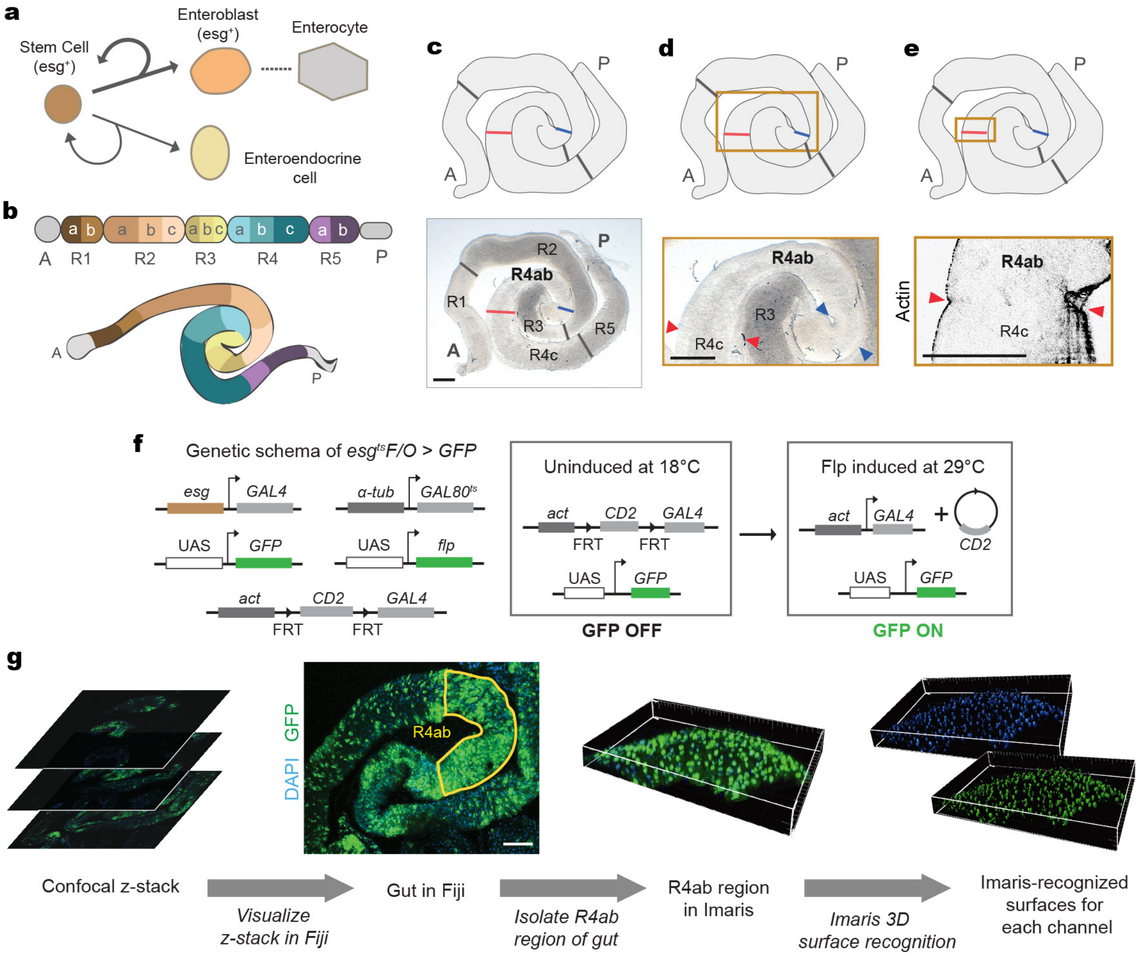

Extended Data Figure 1 | Midgut lineage and morphology, *esg*$^{F/O}$ labelling system and workflow for semi-automated cell counting. **a**, Lineage of the adult *Drosophila* midgut[29,30]. Stem cells are, in general, the only cells capable of division. Asymmetric stem cell divisions typically produce absorptive enterocytes; less frequently, they produce secretory enteroendocrine cells. Enterocytes arise through direct maturation of transient, post-mitotic intermediates called enteroblasts. Stem and enteroblast cells express the Snail-family transcription factor *escargot* (*esg*). **b**, Compartments of the female adult midgut[7,25,31]. The R4ab compartment (also known as P1–2)[25] was used for all experiments in this study. Midgut schematic based on ref. 7. **c**–**e**, Identification of R4ab using morphological landmarks. As defined in ref. 7, R4ab is bounded by the apex of the midgut tube's most distal 180° turn (blue arrowheads in **d**) and the first prominent muscle constriction distal to this 180° turn (red arrowheads in **d**). **e**, The R4ab distal muscle constriction (red arrowheads) is particularly apparent in confocal optical sections. Visceral muscle stained with phalloidin. Midguts in **c**, **d** and in **e** are two different samples. **f**, Genetic schema of the *esg*$^{F/O}$ system[6]. Stem and enteroblast cells are induced to express heritable GFP by temperature shift from 18 °C to 29 °C. The temperature shift inactivates GAL80^{ts}, which allows the stem- and enteroblast-specific *esgGAL4* to drive expression of both *UAS-GFP* and *UAS-flp*. The flp-recombinase renders GFP expression permanent and heritable by excising a CD2 'flp-out' cassette to generate a functional *actGAL4*. Once generated, *actGAL4* drives expression of *UAS-GFP* (and *UAS-flp*) irrespective of cell type. Therefore, after the temperature shift, all mature cells that arise from undifferentiated cells will express *GFP*. **g**, Pipeline for semi-automated, comprehensive cell counts of 3D-reconstructed midgut regions. (1) Confocal microscope *z* stacks capturing the entire depth of the organ are visualized in Fiji. (2) The R4ab region of the midgut (yellow outline) is digitally isolated and exported to Imaris. (Only the top half of the gut tube is shown.) Note that different midgut regions have different rates of turnover: R4ab undergoes complete turnover between adult days 4 and 8 (at 29 °C). However, other regions undergo slower turnover, as shown by large unlabelled regions outside of R4ab (see Methods). (3) To quantify total cells, nuclei (DAPI) are mapped to surface objects using Imaris. To quantify newly added cells in the *esg*$^{F/O}$ system, GFP^{+} cells are recognized in Imaris by co-localization of GFP and DAPI channels, and subsequently mapped to surface objects. Scale bars, 100 μm.

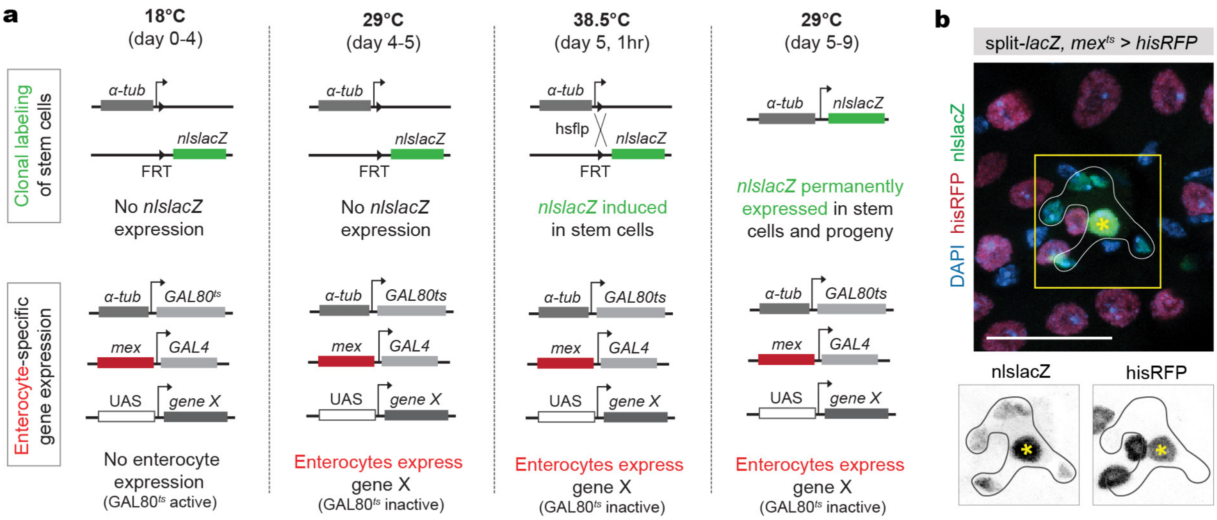

Extended Data Figure 2 | Genetic schema of system to simultaneously manipulate enterocyte expression and trace stem cell divisions. **a**, Detailed explanation of the genetic system in Fig. 1f. Flies are raised at 18 °C; at this temperature, GAL80^{ts} represses *mex*-driven GAL4 in enterocytes (*mex*^{ts}) and lacZ labelling of stem cells is not induced. At four days after eclosion, flies are temperature-shifted to 29 °C; consequent inactivation of GAL80^{ts} allows *mexGAL4* to express genes of interest (*UAS-gene X*) specifically in enterocytes. After one day of UAS gene expression (five days after eclosion), flies are shifted to 38.5 °C for 1 h to induce ubiquitous expression of flp-recombinase, which is under control of a heat-shock promoter (*hs-flp*). Flp catalyses trans-recombination of the two FRTs to place the α-*tubulin* promoter upstream of the promoterless *nls-lacZ* cassette and, consequently, turn on permanent *nls-lacZ* expression. After heat shock, flies are returned to 29 °C to maintain UAS-transgene expression. Midguts are collected for clonal analysis four days after the 38.5 °C heat shock (nine days after eclosion). See Methods. **b**, Validation of genetic system using *mex*^{ts}>*his2av::RFP*. β-Galactosidase marks a stem cell clone (outlined) in a background of His2av::RFP^{+} enterocytes. Within the 5-cell clone, only the enterocyte (yellow asterisk, polyploid) expresses *his2av::RFP*.

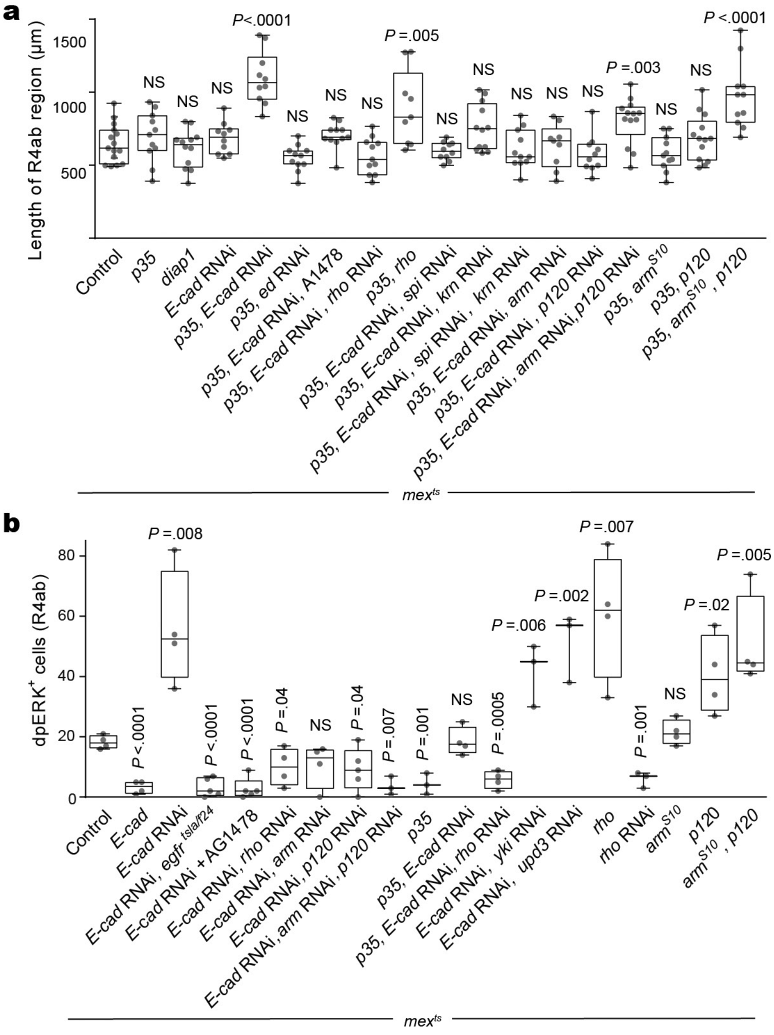

Extended Data Figure 3 | Quantification of organ size and Egfr activation in genetically manipulated midguts. a, Lengths of the R4ab compartment. $n = 15$, 11, 12, 10, 10, 11, 11, 11, 9, 10, 12, 11, 9, 10, 13, 11, 13, and 11 midguts from left to right, analysed after four days of UAS-transgene expression. **b**, dpErk$^+$ cells in the R4ab compartment. $n = 4$, 4, 4, 5, 5, 4, 3, 4, 4, 3, 3, 4, 5, 3, 4, 3, 4, 4, and 4 midguts from left to right, analysed after two days of UAS-transgene expression. One of two replicate experiments was quantified. **a**, **b**, Box-and-whisker plots as in Fig. 1j, k; P values by unpaired t-test compared to control.

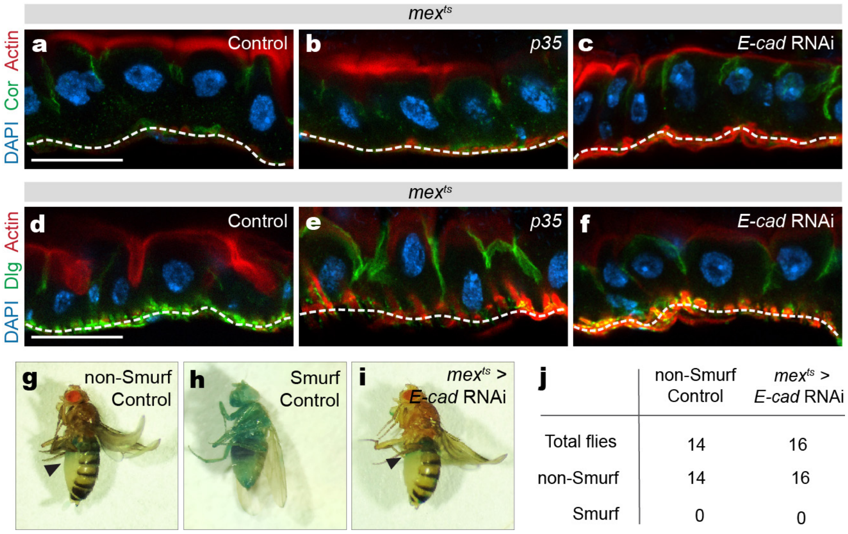

	non-Smurf Control	mex^{ts} > *E-cad* RNAi
Total flies	14	16
non-Smurf	14	16
Smurf	0	0

Extended Data Figure 4 | Analysis of epithelial architecture, polarity and barrier function. a–f, Apoptotic inhibition (**b**, **e**) or *E-cad* depletion (**c**, **f**) in enterocytes does not disrupt either epithelial architecture or apical–basal polarity. Images show vertical sections through the midgut epithelium after four days of either mex^{ts}>*p35* or mex^{ts}>*E-cad* RNAi expression. Enterocytes remain as a coherent monolayer. Apical–basal polarity is intact, as revealed by immunolocalization of apical, actin-rich microvilli (**a**–**f**; SiR-Actin, red) and of two apico-lateral septate junction proteins, Coracle (**a**–**c**, green) and Discs-large (**d**–**f**, green). At the basal surface of the epithelium (white, dotted lines), midgut visceral muscle cells stain brightly for actin and Discs-large. Scale bars, 25 μm. **g**–**j**, Depletion of *E-cad* in enterocytes does not compromize the intestinal barrier. To test the intestinal barrier, flies were subjected to Smurf assays[32] in which a blue, non-absorbable food dye is administered by feeding. The dye remains within the midgut (arrowhead) when the barrier is intact (**g**, non-Smurf), but leaks into the body cavity when the barrier is compromised, such as after the consumption of 1% SDS (**h**, Smurf). After 10 days of mex^{ts}>*E-cad* RNAi expression, midguts still retain the blue dye; no Smurf phenotypes were observed (**i**, **j**).

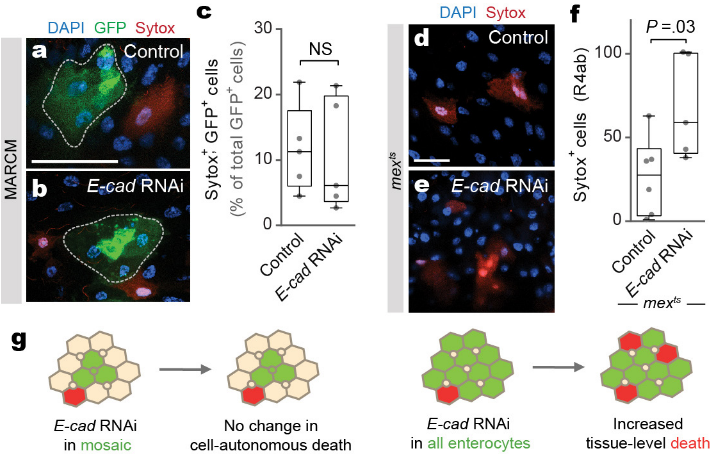

Extended Data Figure 5 | Depletion of *E-cad* has distinct cell-autonomous and tissue-level effects on cell death. In Fig. 2h, total cell counts show that midguts accumulate excess cells when *E-cad* is depleted from apoptosis-inhibited enterocytes, but not apoptosis-competent enterocytes. To shed light on this difference, we examined whether *E-cad* depletion itself promotes cell death. Two approaches, mosaic knockdown and pan-enterocyte knockdown, were used to distinguish direct, cell-autonomous effects from indirect, tissue-level effects. **a**–**c**, Mosaic knockdown of *E-cad* does not promote cell-autonomous death. To generate a mosaic epithelium, MARCM labelling[27] was used to induce sparse, multicellular, GFP-marked clones in a background of unmarked, genetically unperturbed cells. **a**, **b**, Dotted outlines show representative control and *E-cad* RNAi clones (green). Sytox (red) identifies dying cells. **c**, Percentage of GFP^{+} cells that are also Sytox^{+}. Dying cells occur with near-equal frequency within control and *E-cad* RNAi clones. Five midguts per genotype were analysed nine days after clone induction; $n = 873$ cells in control clones and 698 cells in *E-cad* RNAi clones. **d**–**f**, Pan-enterocyte knockdown of *E-cad* promotes cell death, probably through a non-autonomous effect. **d**, **e**, Representative images of *mex*^{ts} control and *mex*^{ts}>*E-cad* RNAi epithelia. Sytox (red) identifies dying cells. **f**, Quantification of Sytox^{+} cells in the R4ab compartment. The number of dying cells increases approximately 2.5× in *E-cad* RNAi midguts compared to control. $n = 5$ midguts per genotype, analysed after three days of transgene induction. **c**, **f**, Box-and-whisker plots as in Fig. 1j, k; P values by unpaired t-test. Scale bars, 25 μm. **g**, Summary. The unaltered frequency of dying cells in *E-cad* RNAi mosaic clones indicates that loss of *E-cad* does not cause cell-autonomous death. This result suggests that increased cell death in *mex*^{ts}>*E-cad* RNAi guts is a non-autonomous, tissue-level effect, possibly due to excess divisions (Fig. 2b) and consequent crowding. These findings may explain why *p35*, *E-cad* RNAi guts accumulate excess cells, whereas *E-cad* RNAi guts retain a normal number of cells (Fig. 2h).

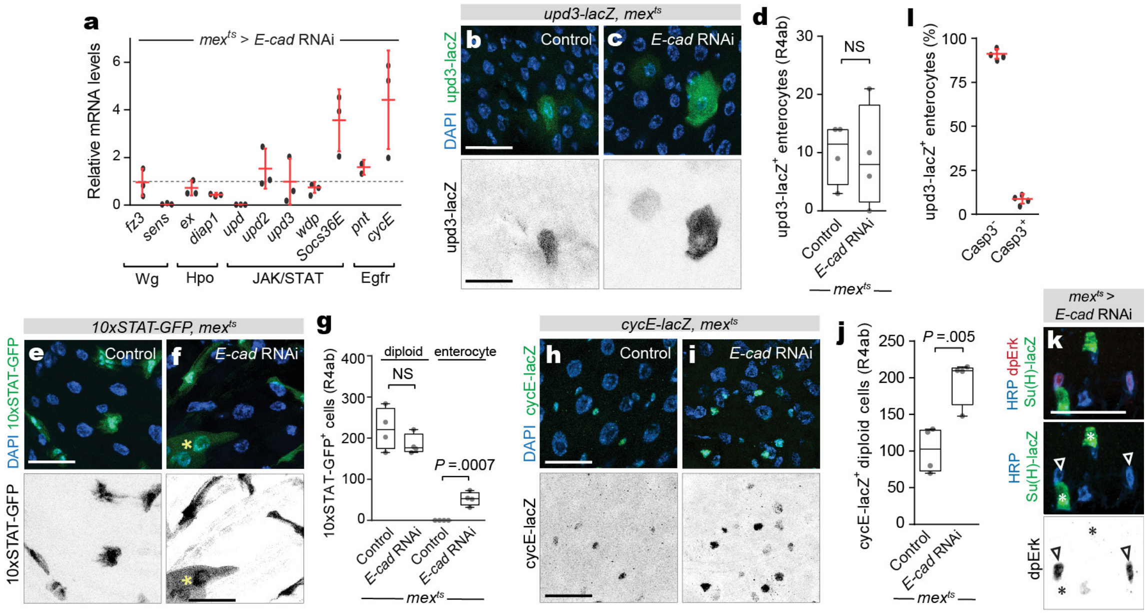

Extended Data Figure 6 | Loss of enterocyte *E-cad* activates Egfr, but not Wg, Hpo or Upd–Jak–Stat. a, Effect of enterocyte *E-cad* depletion on target mRNA expression of known midgut regulatory pathways. mRNA expression was measured by qPCR of *mex^{ts}* control or *mex^{ts}>E-cad* RNAi midguts. Relative to control (dotted line), mRNA expression levels do not increase for the Wg targets *frizzled-3* (*fz3*) and *senseless* (*sens*), the Hpo–Yki targets *expanded* (*ex*) and *diap1*, the injury-associated cytokines *upd* and *upd3*, and the Jak–Stat target *windpipe* (*wdp*). The other Jak–Stat target, *Socs36E*, is increased, which probably reflects its occasional activation in enterocytes (**f**). By comparison, the Egfr target *pointed* (*pnt*) is slightly increased and the Egfr target *cyclinE* (*cycE*) is substantially increased. Values are mean ± s.d.; data points are individual biological replicates analysed four days after induction. **b**–**d**, The number of *upd3-lacZ*$^+$ enterocytes in the R4ab compartment is unchanged by enterocyte *E-cad* depletion. **e**–**g**, The number of *10×Stat-GFP*$^+$ diploid cells in R4ab is unchanged by enterocyte *E-cad* depletion. Occasional activation of *10×Stat-GFP*$^+$ occurs in *E-cad*-depleted enterocytes (asterisk), consistent with increased *Socs36E* (**a**). **h**–**j**, The number of *cycE*$^+$ diploid cells in R4ab increases after enterocyte *E-cad* depletion. **d**, **g**, **j**, Box-and-whisker plots as in Fig. 1j, k; *P* values by unpaired *t*-test; NS, not significant. $n = 4$ midguts per condition, analysed two days after induction. One of two replicate experiments was quantified. **k**, dpErk immunostaining is limited to stem cells (Hrp$^+$, Su(H)lacZ$^-$; arrowheads) and does not mark enteroblasts (Hrp$^+$, Su(H)lacZ$^+$; asterisks), even in *mex^{ts}>E-cad* RNAi midguts. **l**, Expression of *upd3* is not associated with physiological apoptosis. Most enterocytes that express *upd3-lacZ* are non-apoptotic, as assessed by staining for cleaved caspase-3. Values are means ± s.d.; $n = 4$ midguts per condition, analysed six days after eclosion. Representative images are shown in all panels. Scale bars, 25 μm.

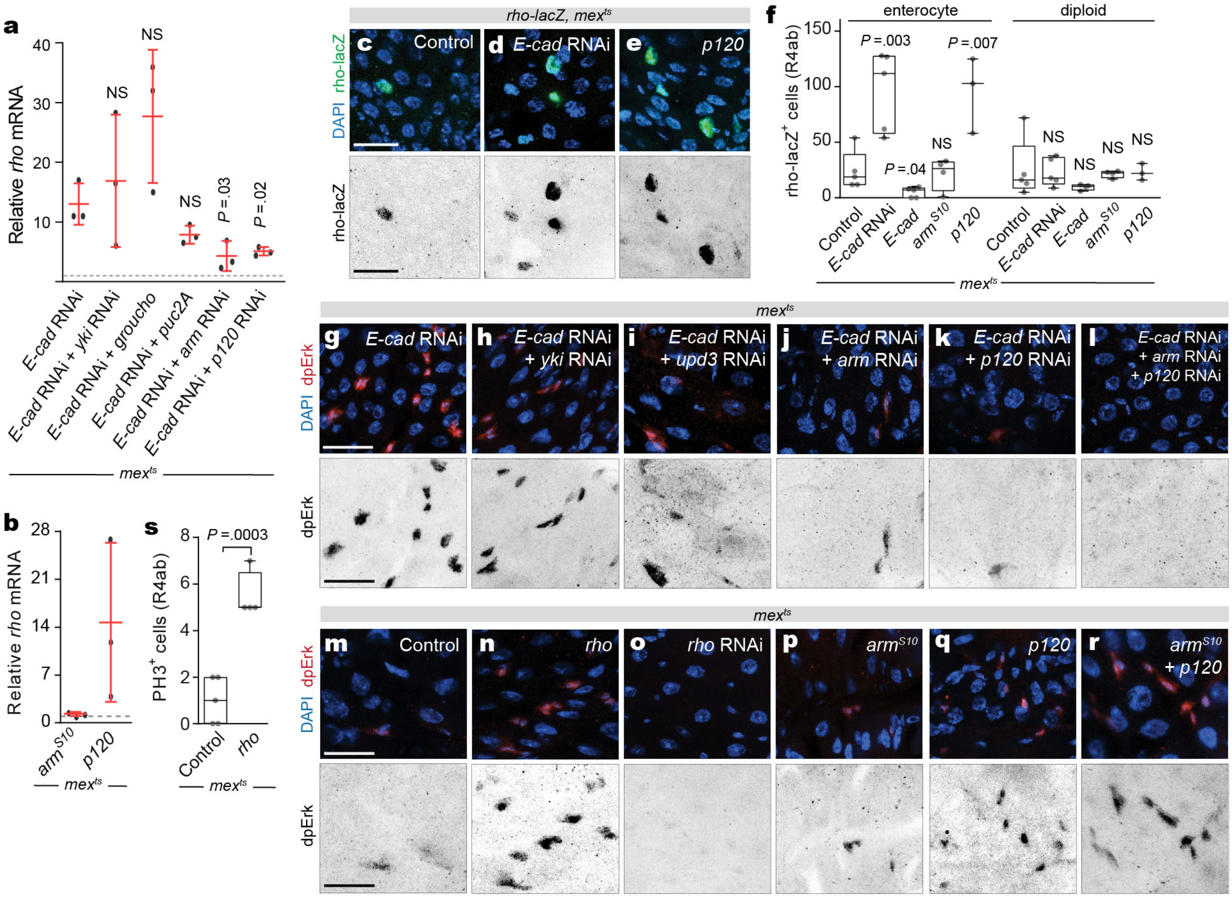

Extended Data Figure 7 | Two E-cad-associated transcription factors, Armadillo and p120-catenin, activate *rho* after loss of *E-cad* in enterocytes. a, *rho* mRNA levels were measured by qPCR of *mex*^{ts}>*E-cad* RNAi midguts with additional manipulation of candidate *rho* regulators as indicated. Five candidates were examined: *yki*, a transcriptional co-activator in the Hpo pathway; *groucho*, a co-repressor known to target *rho* in some tissues[33,34]; *puckered* (*puc*), an inhibitor of Basket/Jnk, the latter of which can enhance Egf signalling; and *arm* and *p120*, co-activators that are inhibited by sequestration at E-cad adherens junctions. Knockdown of either *arm* or *p120* significantly reduces *rho* activation. *P* values by unpaired *t*-test compared to *E-cad* RNAi alone. **b**, Overexpression of *p120*, but not *arm*^{S10}, in enterocytes is sufficient to increase *rho* mRNA levels. **a**, **b**, Values are mean ± s.d.; three biological replicates per condition, analysed four days after induction. Dotted lines show *rho* mRNA levels in unmanipulated controls. **c**–**f**, Depletion of *E-cad* or overexpression of *p120* induces *rho-lacZ* in enterocytes and not in diploid cells. **f**, Quantification. **g**–**l**, Enterocyte *arm* and *p120*, but not *yki* or *upd3*, are necessary for activation of stem cell Egfr (dpErk immunostaining) following loss of *E-cad*. **m**–**o**, Enterocyte *rho* is necessary and sufficient for activation of stem cell Egfr. **p**–**r**, Enterocyte *p120*, but not *arm*, is sufficient to activate stem cell Egfr. See also Extended Data Fig. 3b. **s**, Overexpression of enterocyte *rho* increases the number of mitotic (phospho-histone H3$^+$) stem cells. **f**, **s**, Box-and-whisker plots as in Fig. 1j, k; assessed after two days of transgene expression; *P* values by unpaired *t*-test compared to control; $n = 5, 5, 5, 4$ and 3 midguts from left to right (**f**); and $n = 5$ midguts (control) and 4 midguts (*rho*) (**s**). Representative images are shown in all panels. Scale bars, 25 μm.

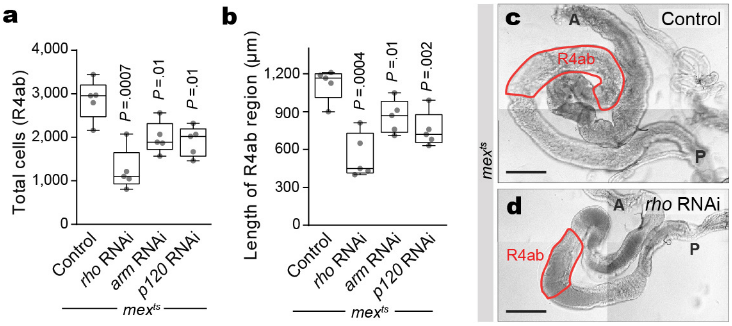

Extended Data Figure 8 | Loss of *rho*, *arm* or *p120* in enterocytes results in organ atrophy. a, Total cell counts. Depletion of *rho*, *arm* or *p120* in enterocytes reduces total cells compared to control. **b**, Depletion of enterocyte *rho*, *arm* or *p120* reduces the length of the R4ab compartment compared to control. **a**, **b**, Box-and-whisker plots as in Fig. 1j, k; $n = 5$ midguts per genotype, analysed after six days of induction; *P* values by unpaired *t*-test compared to control. One of three independent experiments is shown in each graph. **c**, **d**, Depletion of enterocyte *rho* leads to organ atrophy. Representative whole mount images are shown. A, anterior; P, posterior. Scale bar, 200 μm.